Ocean Engineering, Volume 217, December 2020, Article number 108016
DOI: 10.1016/j.oceaneng.2020.108016

Water entry of slender segmented projectile connected by spring

Zhengyang Wu[a], Chengchun Zhang[a,b,*], Jing Wang [c], Chun Shen[b], Liang Yang[d], Luquan Ren[a]

[a] *Key Laboratory of Bionic Engineering (Ministry of Education), Jilin University, Changchun 130022, China*

[b] *State Key Laboratory of Automotive Simulation and Control, Jilin University, Changchun,130022, China*

[c] *College of Physics, Jilin University, Changchun 130012, China*

[d] *Centre for Renewable Energy Systems, Cranfield University, Cranfield, MK43 0AL, United Kingdom*

Abstract

An object that enters the water experiences a large impact acceleration at the initial stage of water entry, which can cause structural damage to objects that are dropped or launched into the water. To reduce the peak impact acceleration, a spring-connected segmented projectile with compressible nose was designed. Through inertial measurement unit and high-speed camera, the influence of the nose compressibility on the initial impact acceleration was qualitatively investigated. The experimental results demonstrate that the introduction of a spring between the nose and the main body of the projectile can significantly suppresses the peak acceleration during the early stage of impact (0-50 ms). Furthermore, the maximum impact acceleration experienced by the main body is only related to the maximum compression of the nose without considering the spring stiffness. In addition, using the spring exerts a slight effect on the non-dimensional pinch-off times of the cavity but increases the initial velocity required for the occurrence of cavity pinch-off events on the side of the main body.

Keywords: segmented projectile, spring, water entry, impact acceleration reduction, cavity dynamics

1. Introduction

Studies of the water entry events of objects have been conducted for more than 100 years, and began with the first image of water droplets falling into a water-milk mixture photographed by Worthington and Cole (1897). This has been widely covered in different fields, including military applications such as missile water entry (May, 1975), civilian applications such as ship slamming (Tveitnes et al., 2008), aerospace engineering applications such as the design loads of spacecraft water entry (Hirano and Miura, 1970), and bio-specific functional mechanisms such as plunge-dive gannets

Published by Elsevier. This is the Author Accepted Manuscript issued with: Creative Commons Attribution Non-Commercial No Derivatives License (CC:BY:NC:ND 4.0).
The final published version (version of record) is available online at DOI:10.1016/j.oceaneng.2020.108016. Please refer to any applicable publisher terms of use.

(Wang et al., 2013). The main research contents of water entry focus on the formation and evolution of the cavity (Lee et al., 1997; Bergmann et al., 2009; Duclaux et al., 2007), the trajectory of objects (Dupeux et al., 2010; Rosellini et al., 2005; Truscott and Techet, 2009), and the calculation of the impacting load (Korobkin and Pukhnachov, 1988; Korobkin and Scolan, 2006; Alaoui et al., 2015). This study presents an experimental study of the impact of a slender segmented projectile, spring-connected on a free surface. This study offers the first examination of how a compressible projectile nose affects the water-entry phenomenon, especially the impact force on the main body of the projectile.

In general, the water entry of objects can be divided into two categories: cavity forming and non-cavity forming. The major parameters that determine whether a cavity is formed include the capillary number $\mathrm{Ca} = \mu U_0/\sigma$, wetting angle, and geometry (Duez et al., 2007; Truscott and Techet, 2009b). Furthermore, the larger the capillary number (high impact speed) and wetting angle, the more likely a cavity forms. The four typical types of cavities include surface seal, deep seal, shallow seal, and quasi-static seal (Aristoff et al., 2008; Aristoff and Bush, 2009) depending on the depth at which pinch-off occurs when a cavity forms. Among these types, the deep seal appears in most water entry cases and is characterized by the first pinch-off event, which occurs much closer to the sphere, typically at one-third to one-half of the distance between the sphere and the undisturbed free surface (Aristoff and Bush, 2009). To characterize the deep seal event, the important parameter of the non-dimensional pinch-off time, $t^* = U_0 t / D$, was used by Aristoff et al. (2010). Furthermore, the results show that the non-dimensional pinch-off times remain constant and independent of both impact velocity and mass ratio. Moreover, another non-dimensional pinch-off time, $\tau = t\sqrt{2g/D}$, was proposed by Glasheen and McMahon (1996) is used as well. Cavities with deep seal, which always form after water entry due to the slender geometric shape and the non-dimensional pinch-off times, were also examined in the present study.

The main source of the impact force during the initial stage of water entry is the added mass (Von Karman, 1929). Von Karman (1929) was the first to theoretically study the impact forces on seaplane floats during water entry and introduced the concept of added mass by assuming that the momentum of the water/body system is conserved. Wagner (1932) further developed the theory of Von Karman

(1929) by considering the effects of the change in boundary conditions including the calculation of the piled-up water surface and the spray thickness. Subsequently, most theoretical studies (Yu, 1945; Shiffman and Spencer, 1951; Grady, 1979) on the impact force of water entry are based on their research. In addition to the added mass, the water hummer (Korobkin and Pukhnachov, 1988), which is generated at the sphere initially touches the water surface, is also one of the sources that contribute to the initial impact force. Furthermore, the formation of a high-speed radial jet greatly increases the initial impact force on the sphere as reported by Thoroddsen et al. (2004). Prior research (Shiffman and Spencer, 1945; Grady, 1979) on object impact on a water surface showed that a large peak acceleration exists during the very early stage of water entry. This may even appear at the time when the sphere is submerged between 10% and 20% of its radius (Moghisi and Squire, 1981).

To reduce the impact force, several studies have recently been conducted. Bodily et al. (2014) studied the effect of the nose shape of slender axisymmetric bodies on the peak impulsive force. The results showed that projectiles with cone-nose shape suffered the smallest impact force compared to other nose shapes. Chang et al. (2016) investigated the stability of the seabird's neck during plunge-diving. They simplified the bird system as a long, thin, elastic beam that is attached to a rigid cone, which represent the bird's neck and head, respectively. The result indicates that the axial force acting on the neck of the bird increases with the skull radius, especially the beak angle. Speirs et al. (2019) proposed a method to reduce the initial impact force experienced by a sphere during water impact by using a jet of water, which strikes the free surface prior to sphere impact. Introduction of this jet accelerates the previously static water and reduces the added mass effect on the impacting body. The force could be reduced by 75%, using this method.

It is self-evident that the appearance of the large impact force at the initial stage of entering water, as mentioned above, will cause both structural damage and internal component failure of objects. This study designed a segmented projectile with spring-connection with the primary aim to reduce the impact force. We expect that the peak force can be reduced by converting the kinetic energy induced by the impact of the free surface into potential energy of the spring. For quantitative analysis, to assess the influence of the introduction of spring on the initial impact force, an inertial measurement unit (IMU) was used to record the impact acceleration. Moreover, to study the cavity dynamics, a

high-speed camera was used to capture the impact event of the projectile during water entry. The experiment was carried out at a lower speed range and the water entry of a nose fixed projectile were used as comparative test.

2. Experimental methods

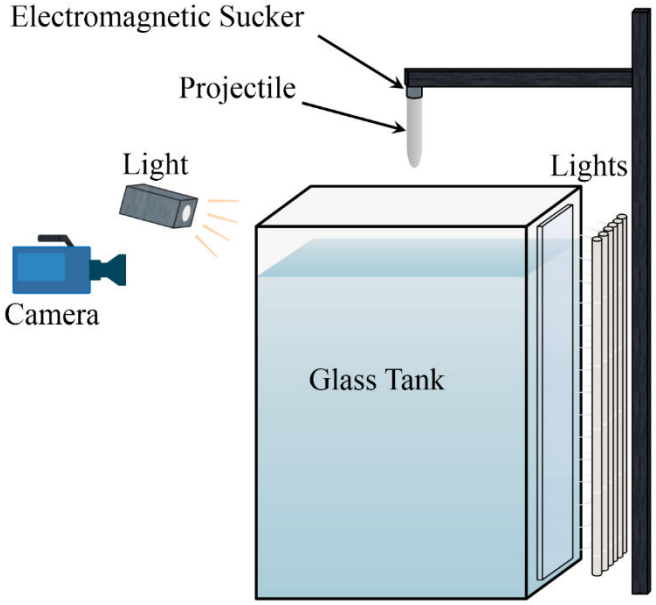


Fig. 1. Schematic view of the experimental apparatus.

Fig. 1 shows the experimental apparatus used for this study. The projectile was fixed on an electromagnetic sucker via iron sheet, which was stuck in the tail of the projectile. The initial impact velocity was controlled by varying the height between the tip of the nose of the projectile and the free surface. When the power of the electromagnetic sucker was interrupted, the projectile was released from the rest and fell freely toward the glass tank measuring 70 × 70 × 100 cm (width × depth × height) filled with water to 80 cm. Six different drop heights H_0 were used to vary the initial impact velocity close to $U_0 \approx \sqrt{2gH_0}$ by ignoring the air drag. U_0 can also be determined through analysis of video sequences. A high-speed camera (Phantom V711, Vision Research, Inc.) that was positioned normal to the tank was utilized to capture the impact event of the projectile at a rate of 4000 frames/s with 1280 × 800 pixels. The conversion factor between mm and pixels is 0.526 mm/pixels. Six 36 W LED fluorescent tubes with a diffuser sheet were used to provide backlighting for the camera images and were placed behind the tank. A 1000W LED floodlight was used to provide the foreground lighting and

was placed in front of the tank.

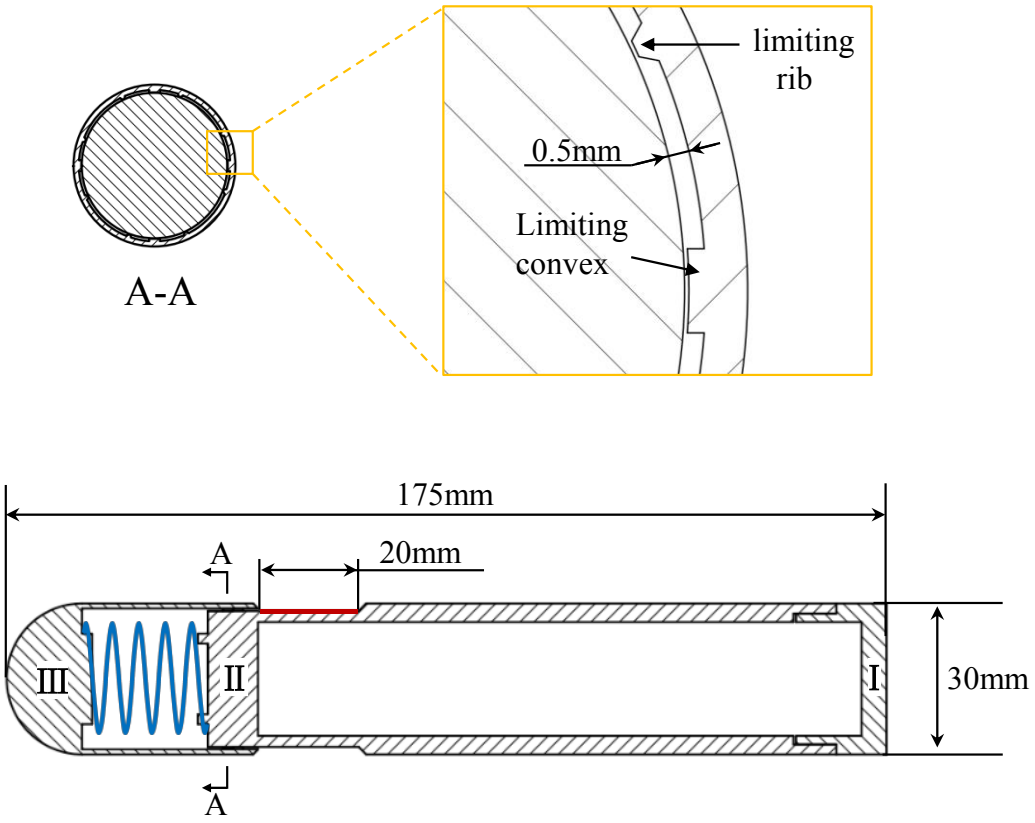


Fig. 2 Schematic diagram of geometric parameters of the projectile. A-A shows the section view and the yellow rectangular box shows a local enlargement.

To quantitatively analyze the influence of compressibility of the projectile nose on the water entry impact force and cavitation dynamics, a three-segment projectile including tail (I), main body (II), and nose (III) was designed, as shown in Fig. 2. The main body had a length of 125 mm and two outer diameters. The end with an outer diameter of 30 mm is connected to the tail and the other end with an outer diameter of 27 mm, which is connected to the nose. A cylindrical cavity with an inner diameter of 22.6 mm and a length of 120 mm is formed after the main body and the tail are connected and is used to place the block weight, IMU, and spacers. The order of the block weight, IMU, and spacers is shown in Fig. 3. The block weight is placed at the bottom of the main body with the IMU is situated above. This moves the center of mass as close as possible to the nose of the projectile to minimize the projectile rotation and lateral displacement during water entry (Bodily et al., 2014). The nose of the projectile has a hemispheric nose shape with an outer diameter of 30 mm, an inner diameter of 28 mm, and a length of 50 mm. Eight limiting ribs were uniformly arranged on the inner-wall of the nose to ensure that the

nose moves only along the axis of the main body when assembled. Four limiting convexes were uniformly arranged on the inner-wall of the nose and the outer-wall of the main body, to limit the position between them and to ensure that the nose does not slip from the projectile during testing. The gap between the limiting rib and the outer-wall of the main body was 0.05 mm, which ensures high axiality. A spring with a 20 mm maximum compression length was installed between the nose and the main body, which is also the maximum sliding length (marked with the red line in Fig. 2) of the nose along the main body. The main parameters of the spring are listed in Table 1. The projectile used in this study was made by 3D printing technology using UV Curable Resin. This provides a hydrophilic surface with a wetting angle $\theta = 79 \pm 5°$ and surface roughness $R_z = 7.8 \pm 1.2$ μm.

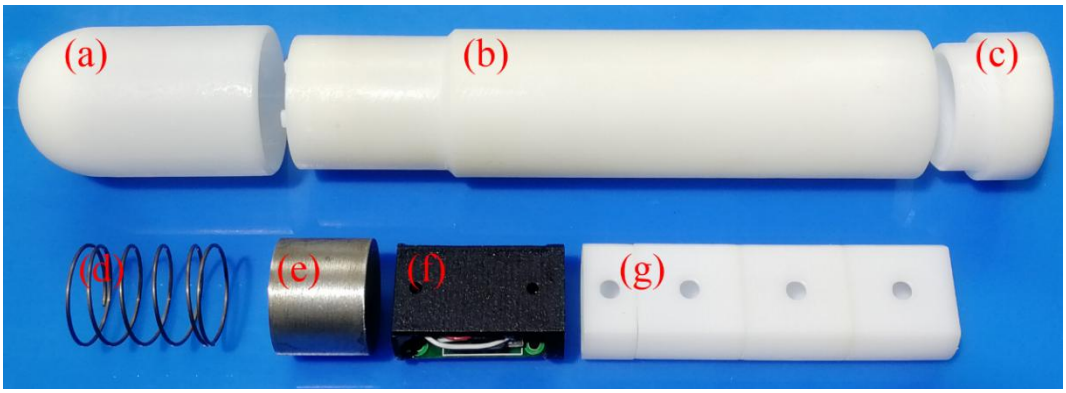


Fig. 3 Physical splitting chart of the projectile. (a) Nose. (b) Main body. (c) Tail. (d) Spring. (e) Block weight. (f) Inertial measurement unit (IMU). (g) Spacers.

The IMU has a three-axis accelerometer and was used to record the instantaneous acceleration that the projectile experienced during water entry at a rate of 2000 Hz. The accelerometer is an ICM42605 motion tracking device manufactured by InvenSense Inc. and was set to a maximum range of ±16 g with a measurement error of 0.01 g.

Table 1. The main parameters of the spring

Material	Stiffness (N/mm)	Line diameter (mm)	Outer diameter (mm)	Free length (mm)
Stainless steel	0.1	0.8	19.6	25

Two forms of projectiles were used in this study. For the first form, the nose was fixed on the main body through a sealant, which avoided the relative displacement between the nose and the main body during the test. This form was called Nose Fixed Projectile (NFP). For the second form, the nose and

the main body are not fixed. During the initial stage of impact, the nose is decelerated by a large hydraulic impact pressure, while the main body continues to accelerate while falling due to its large inertia. Relative motion occurs between them, which results in axial compression of the spring. It can be considered that the nose is compressed relative to the main body. This form was called Nose Compressible Projectile (NCP). Both forms of projectile have the same total length of L = 175 mm and density of ρ = 1.12 g/cm^3 before impacting the free surface.

Table 2. Initial water entry initial condition for the projectile

H_0 (m)	U_0 (m/s)	Reynolds	Weber	Froude
0.1	1.40	46879	814	2.58
0.2	1.98	66296	1628	3.65
0.3	2.43	81196	2442	4.47
0.4	2.80	93757	3256	5.16
0.6	3.43	114829	4884	6.32
0.8	3.96	132593	6511	7.30

In this study, three non-dimensional parameters, Reynolds number $\mathrm{Re} = \rho_w U_0 D / \mu$, Weber number $We = \rho_w U_0^2 D/\sigma$, and Froude number $Fr = U_0 / \sqrt{gD}$ were used to characterize the water entry of the projectile. Here, ρ_w represents the water density, D represents the radius of the projectile, μ represents the dynamic viscosity of the water, σ represents the surface tension, and g represents the acceleration due to gravity. The parameters used in this study are listed in Table 2.

At least five effective tests were conducted at each height for each form of projectile. The compression of the nose relative to the main body during water entry of NCP, which is also a spring compression, was measured in pixels from the recorded images, and the uncertainty of measurement from the pictures is ±1 pixel (corresponding to ±0.5 mm). All tests were conducted at atmospheric pressure and room temperature (about 25 °C).

3. Results and discussion

3.1. Cavity dynamics and projectile acceleration

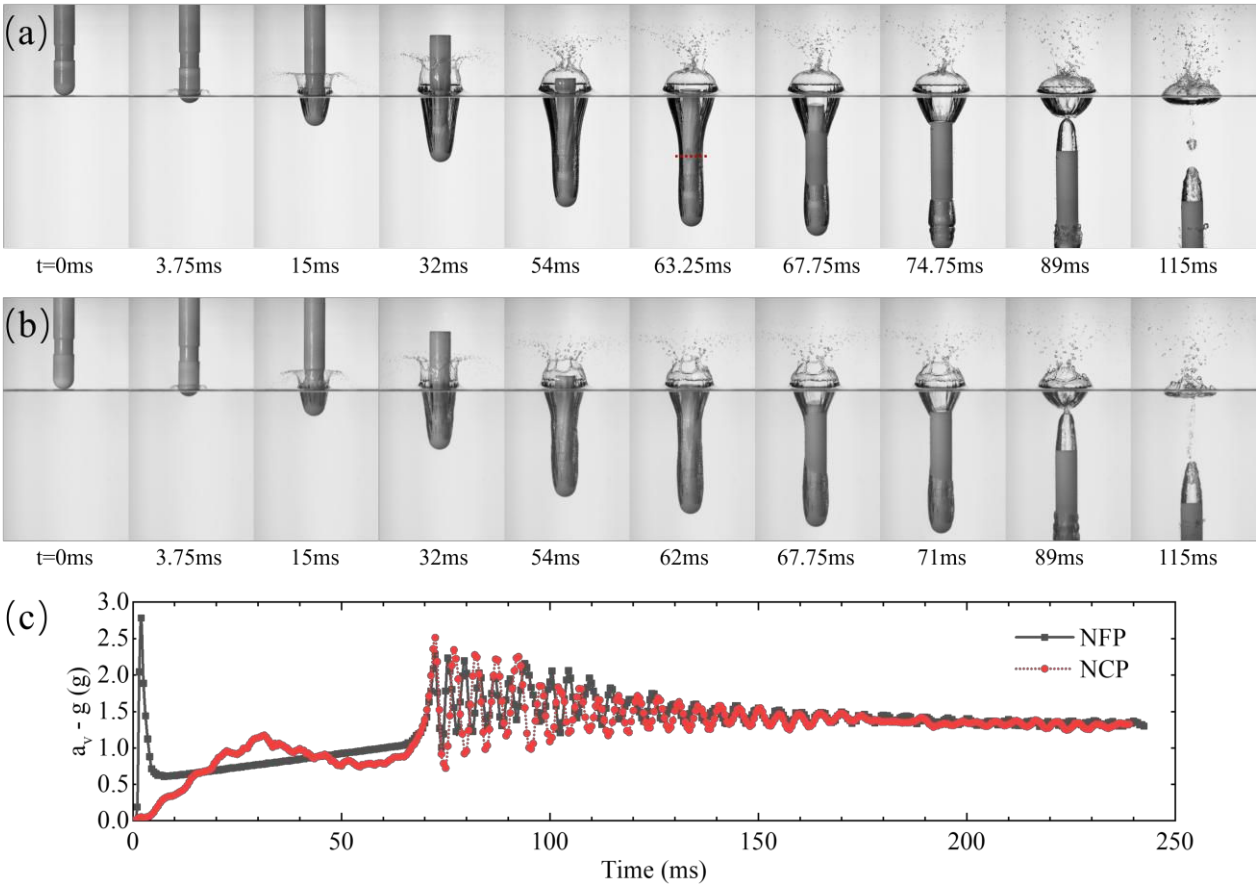


Fig. 4 Image sequence of water entry and corresponding axial impact acceleration. (a) NFP impacts free surface at a velocity of U_0 = 2.80 m/s. (b) NCP impacts free surface at the same velocity of U_0 = 2.80 m/s. (c) The axial impact acceleration $a_v - g$, normalized by g versus time for NFP and NCP impacting the free surface in (a) and (b).

Fig. 4(a) and (b) show the image sequence of the NFP and NCP impacting the free surface at the same initial velocity of U_0 = 2.80 m/s. Fig. 4(c) shows the corresponding axial impact acceleration, normalized by g, where the axial impact acceleration is the real acceleration a_v minus the gravity g. For the NFP water entry, an initial horizontal jet of fluid forms as the projectile impacts the free surface, followed by the formation of a vertical splash crown as the nose of the projectile penetrates the water. With decreasing air pressure in the cavity, the splash crown moves inward. At the time of 54 ms, a surface closure occurs behind the tail of the projectile. However, in the test of higher initial velocity (U_0 = 3.43 m/s and 3.96 m/s), the surface closure appears first on the side of the projectile and then

again on the tail, as shown in Fig. 5. At 63.25 ms, a deep seal of the main cavity occurs on the side of the projectile, generating a three-phase contact line of the air-water-projectile. Then, the contact line is divided into two and moves fast in the opposite direction along the side of the projectile with the main cavity split into two separate cavities. The lower cavity remains attached to the forehead of the projectile when the contact line moves to the shoulder of the main body and oscillates as the projectile enters deep into the water. At the same time, another contact line moves quickly to the tail of the projectile and is attached to the edge of the tail. At the time of ~89 ms, the second-deep seal happened with the upper cavity pinch-off behind the tail of the projectile. Two separate cavities generate again, where the upper cavity is connected to the free surface and the lower cavity is attached to the tail of the projectile. Ripples in the tail cavity are seen similar to when a sphere enters the water as described by Grumstrup et al. (2007). Then, vortex shedding begins and a bubble separates from the tail cavity and rises to the water surface. The black dotted line shows the corresponding NFP axial impact acceleration curve versus time. During the very early stages of impact (0-10 ms) an acceleration spike appears first due to the nose of the projectile accelerating a portion of the surrounding water (added mass) (Shiffman and Spencer, 1945). A linear increase of the acceleration followed until about the time of 63.25 ms, when the pinch-off of the main cavity occurred on the side of the projectile. Then, the acceleration increased sharply and another peak of the acceleration appeared at the time of ~74.75 ms, which is the moment when the contact line moves to the edge of the tail. During this time (63.25-74.75 ms), the main cavity collapses on the side of the projectile. The contact area between the fluid and the projectile increases, resulting in the increase of viscous drags and differential pressure drags of the fluid on the projectile. Then, a periodic acceleration oscillation appears, which is caused by the disturbance of the surrounding fluid due to the collapse of the upper cavity and the oscillation of the tail cavity.

When NCP enters the water, compared with NFP a weaker jet of fluid, followed by a smaller cavity, formed at the initial stage of impact. Compression begins between the nose and the main body, which are connected by a linear spring. At the time of ~32 ms, the compression of the nose achieved maximum (~11.86 mm). At the time of 62 ms, pinch-off occurs on the side of the projectile. The subsequent evolution trend of the cavity is basically identical to that of NFP. Throughout the water

entry process, the size of the cavity formed by NCP entering water is clearly smaller than that of NFP and the splash crown remains open without forming a dome. The red dotted line is the corresponding NCP axial impact acceleration curve versus time. This acceleration is the measured value of the main body of the projectile. Compared to the acceleration curve of NFP, the acceleration spike disappeared during the very early stages of impact and were replaced by a gradually increasing acceleration from 0 ms to about 32 ms. Then, a slight decline in acceleration occurred, followed by a sharp increase in acceleration at ~62 ms. A peak of the acceleration appeared at the time of ~71 ms, which is also the moment when the contact line moves to the edge of the tail. The subsequent variation trend and magnitude of acceleration are basically consistent with those of NFP. As the use of the spring between the nose and the main body of the projectile significantly suppressed the peak impact acceleration during the early stage of impact (0-50 ms) and exerted little effect on the subsequent acceleration, the following mainly focused on this period of the impact.

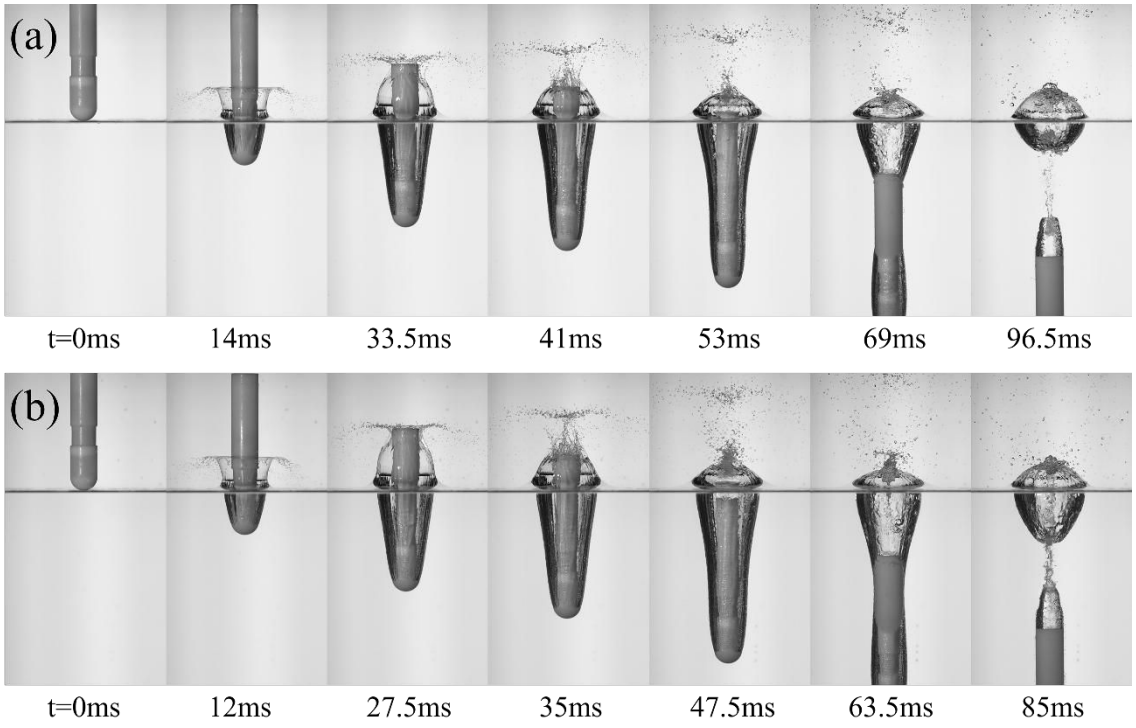


Fig. 5 Image sequence of water entry for NFP. (a) U_0 = 3.43 m/s, the surface closure appears first on the side of the projectile at the time of 33.5ms and then again on the tail at the time of 53ms. (b) U_0 = 3.96 m/s, the surface closure appears first on the side of the projectile at the time of 27.5ms and then again on the tail at the time of 47.5ms.

3.2. Effects of the initial velocity on the impact acceleration of projectile

Fig. 6(a) and (b) show the axial impact acceleration, normalized by g, as experienced by both projectiles (NFP and NCP) during the early stage of impact under the conditions of six different initial velocities. In order to measure the peak impact acceleration more accurately, at least 5 effective tests have been carried out at each height for NFP and NCP. Here, the effective test refers to the test that the projectile does not rotation and lateral displacement during water entry. The data used in Fig. 6 are the mean values of five effective tests. For the NFP impacting water, two stages of impact acceleration could be separated. The first stage was 0-10 ms, when the peak acceleration occurred at ~1.5 ms and the relationship between the maximum acceleration a_{max} normalized by g and the initial impacting velocity U_0 is quadratic. Therefore, a second-order curve can be used to fit the variation of a_{max}/g with U_0 as shown in Fig. 7, where the error bars represent the standard deviation which is also used in other graphs in this paper. To be clear, due to the sampling rate is not high enough, the timing and magnitude of peak acceleration shown in Fig. 6 may not reflect the true peak. The second stage is 10-50 ms, and the acceleration increases linearly with approximately the same growth rate at different initial velocity. At the moment of 30 ms, the axial acceleration was plotted as a function of U_0 in Fig. 8 to show the relationship between them during the second stage. A linear curve was found to fit them well. When the NCP impacts water, no peak impact acceleration appeared in all initial impact velocity tests. Within the time of about 0-5 ms, a small increase in acceleration can be seen. Then, within 5-20 ms, the acceleration increased approximately linearly. Next, the acceleration started to slow down at the period of 20-32 ms. At the time of ~32 ms, the acceleration reached its maximum and the time it took for the NCP entry water to reach the maximum acceleration is basically independent of the initial impact velocity U_0. A slight decrease in acceleration occurred within 30-50 ms except for the test of U_0 = 1.40 m/s. It should be noted that the acceleration curve is not smooth for the NCP entry water, but has slight fluctuation. The main reason is that a tiny but discontinuous friction force is generated between the nose and the main body when it is compressed, which acts on the main body, resulting in the fluctuation of acceleration during water entry. In comparison, the maximum impact acceleration a_{max} normalized by g experienced by NCP in the initial stage of impact is also plotted in Fig. 7. The relationship between a_{max}/g and U_0 is linear for the NCP impact. Moreover, the difference of maximum

impact acceleration between both projectiles increased significantly with increasing initial velocity U_0. This shows that the effect of the spring on the reduction of the maximum impact acceleration of the high-speed projectile is stronger during the early stage of impact.

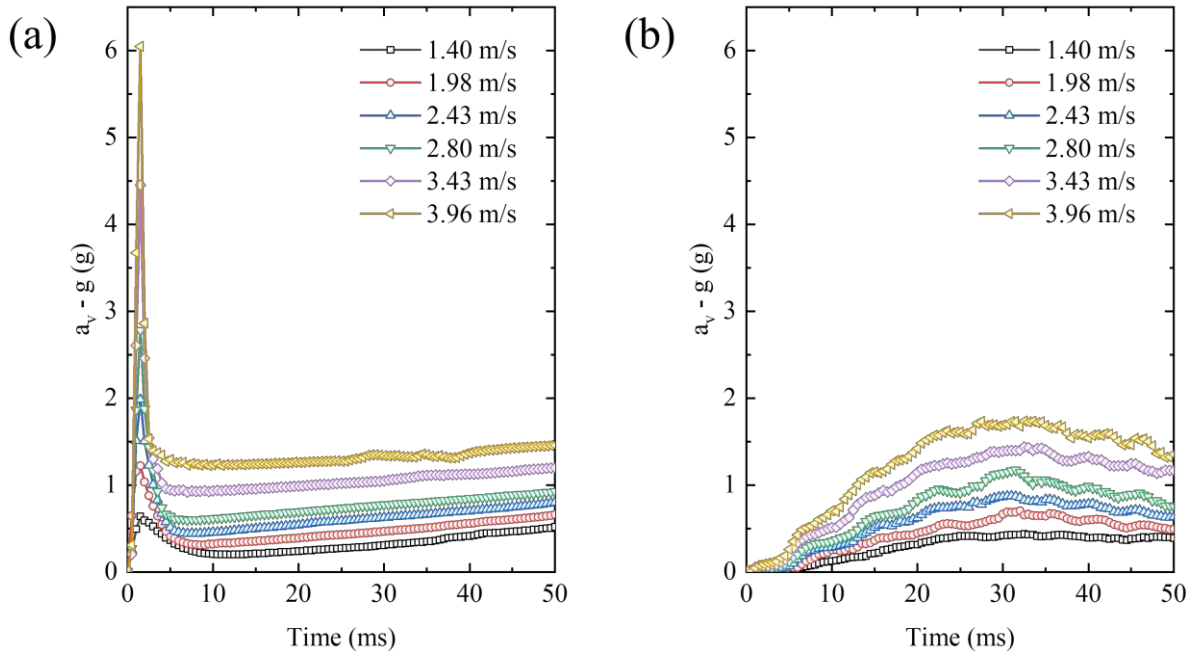


Fig. 6 Time history of the axial impact acceleration, normalized by *g* under the conditions of six different initial velocities. (a) NFP impacts free surface. (b) NCP impacts free surface.

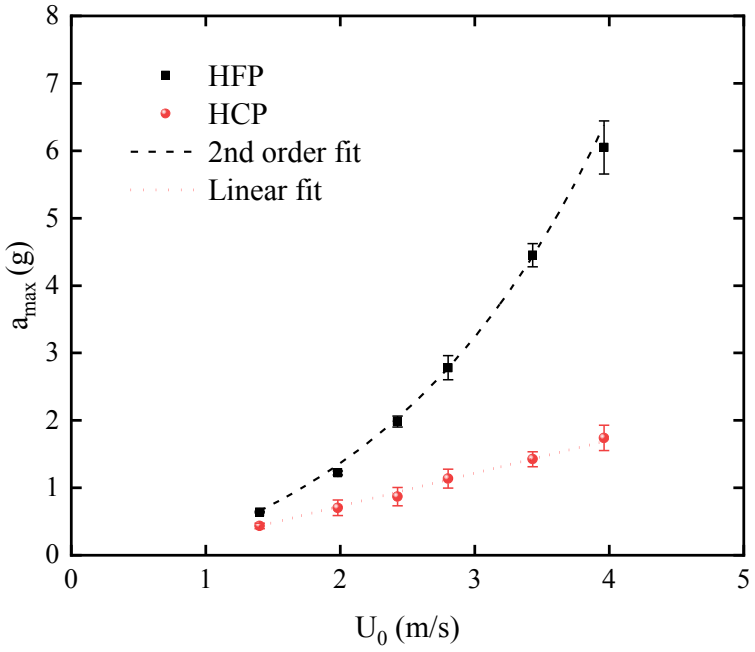


Fig. 7 Maximum acceleration a_{max}, normalized by *g* as a function of the initial velocity U_0 for NFP and NCP during the initial stage of impact.

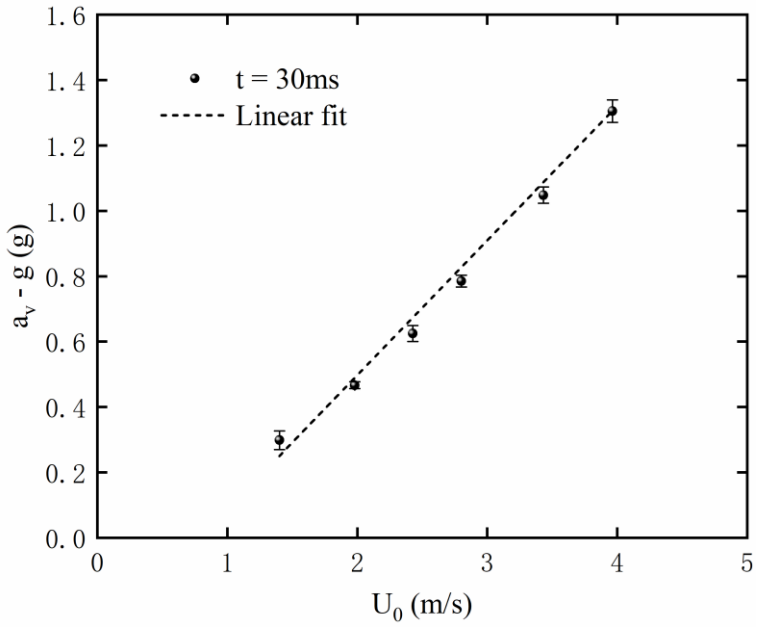


Fig. 8 Axial impact acceleration, normalized by *g* as a function of the initial velocity U_0 for NFP at the moment of 30 ms.

3.3. Cavity pinch-off

As mentioned in Section 3.1, two deep seals occur at the impacting event of U_0 = 2.80 m/s, one of which occurs on the side of the projectile and the other occurs behind the tail of the projectile. Clearly, the deep seal occurring on the side of the projectile greatly influence the formation and development of the second peak acceleration. Furthermore, the occurrence of deep seal behavior on the side of the projectile may also exert an effect on the initial impact acceleration. Therefore, the non-dimensional pinch-off times ($t^* = U_0 t / D$) for both forms of projectiles were used to characterize the two deep seal events. Figure 9 shows the relationship between the non-dimensional pinch-off time t^*_a and t^*_b versus the Froude number, where t^*_a represents the non-dimensional time of the main cavity pinch-off on the side of the projectile, and t^*_b represents the non-dimensional time of pinch-off behind the tail of the projectile. The used of the spring between the nose and the main body of the projectile slightly affected the non-dimensional pinch-off times t^*_a and t^*_b. Furthermore, the non-dimensional pinch-off time t^*_a increased linearly with the Froude number; however, there is no clear relationship between t^*_b and the Froude number. The single value of dimensionless pinch-off

time, $\tau = t\sqrt{2g/D}$, was also calculated. The values for NFP and NCP pinch-off on the side of the projectile were τ_{a-NFP} = 1.573 ± 0.0621 and τ_{a-NCP} = 1.513 ± 0.0628, which are almost equal to the value of τ_A = 1.530 ± 0.155 as reported for a cone nose shape projectile by Bodily et al. (2014). Moreover, at the velocity of U_0 = 1.98 m/s, no pinch-off events occurred on the side of the projectile for NCP entry water. This is because the deformation of spring absorbed the partial inertia, which is required by the nose cavity forms. Therefore, the use of spring increased the initial velocity required for the occurrence of pinch-off behavior on the side of the projectile.

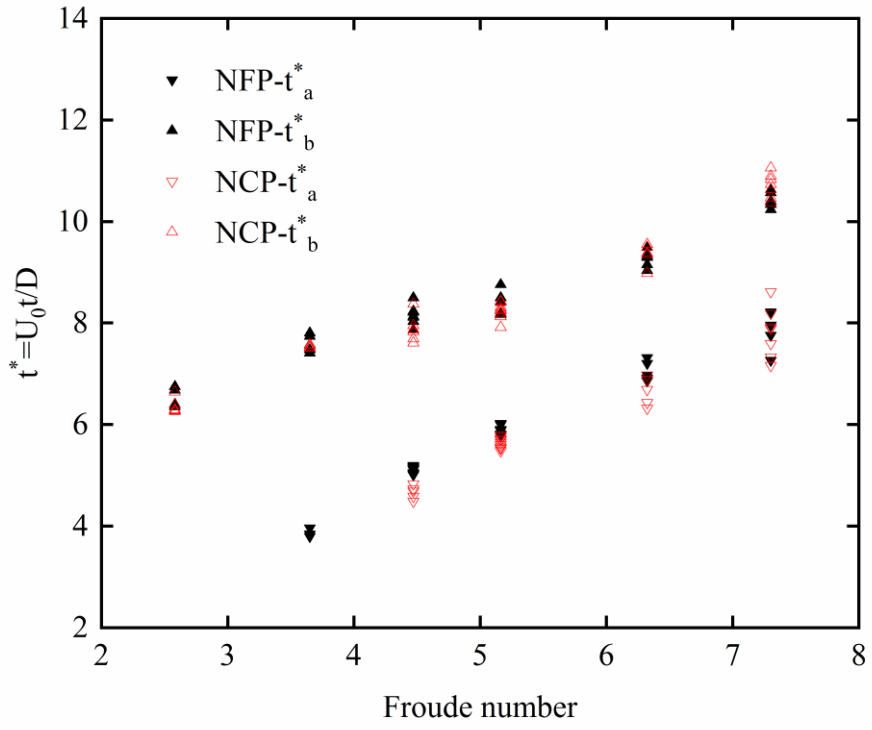


Fig. 9 Non-dimensional pinch-off time as a function of the Froude number for NFP and NCP.

3.4. Compression of the nose for NCP

The most intuitive phenomenon corresponding to the reduction of the maximum acceleration of the NCP during the early stage of impact is the compression of the nose. Fig. 10 shows the time history of the amount of nose compression (ΔL) for NCP during the early stage of impact under the conditions of different initial velocities. ΔL is also the amount of spring deformation. At the beginning of 2.5 ms, the compression of the nose is small. Within the time of ~2.5-20 ms, the nose compression increased

approximately linearly and then slowed down until it reached its maximum at about 32.5 ms. Finally, the compression decreased slightly after remaining constant for a period of time. However, it should be noted that the compression may have reached the maximum compression length (20 mm) of the spring between approximately 30-40 ms at the velocity of U_0 = 3.93 m/s due to potential combined manufacturing tolerances and deflection measurement accuracy, although the compression measured by us is less than 20 mm. The variation trend of the nose compression with time at different initial velocities is basically identical to that of the impact acceleration experienced by the NCP during the early stage of impact when entering the water. Furthermore, the time when the amount of the nose compression reached its maximum value ΔL_{max} basically remained the same as the time when the impact acceleration reached its maximum value. The slight time difference could be attributed to the lack of the sampling data of compression at the time of 32 ms. Fig. 11 shows the relationship of the maximum compression ΔL_{max} and the initial velocity U_0. The maximum compression increased linearly with increasing initial velocity. Fig. 12 shows the instantaneous water entry events of NCP with different initial velocities at a time of 32.5 ms. At the low speed (1.40 m/s and 1.98 m/s), although no cavity appeared in the nose of the projectile, the water did not touch the main body of the projectile due to the low depth of penetration. At relatively high initial velocities, there is also no contact between the water and the main body due to the formation of the cavity. This significantly simplified the analysis of the force that acts on the main body of the projectile during the early stage of impact.

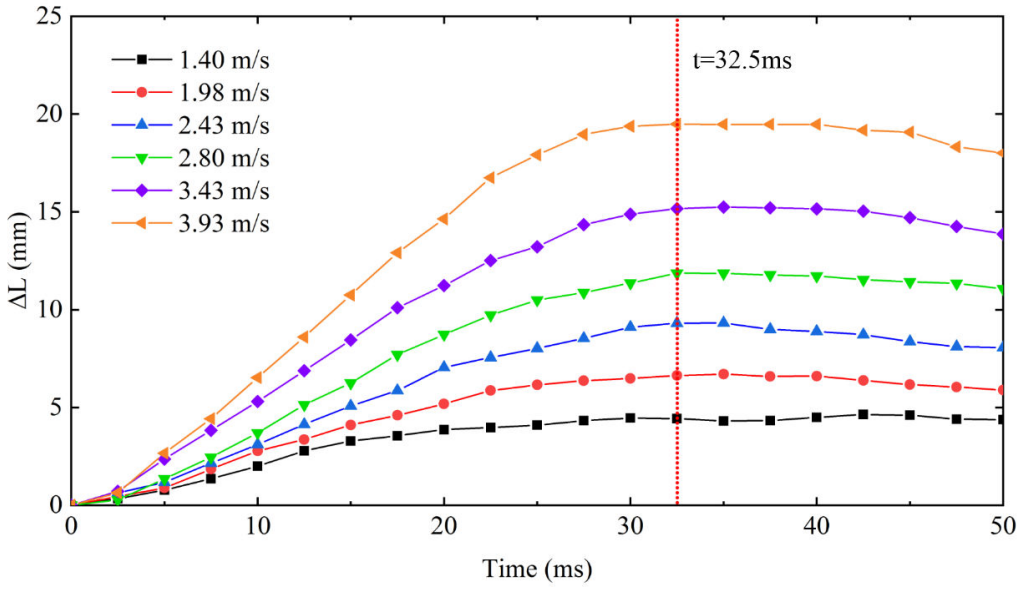


Fig. 10 Time history of the amount of nose compression ΔL for NCP under the conditions of six different initial velocities. The red dotted line indicates the time required to reach the maximum compression.

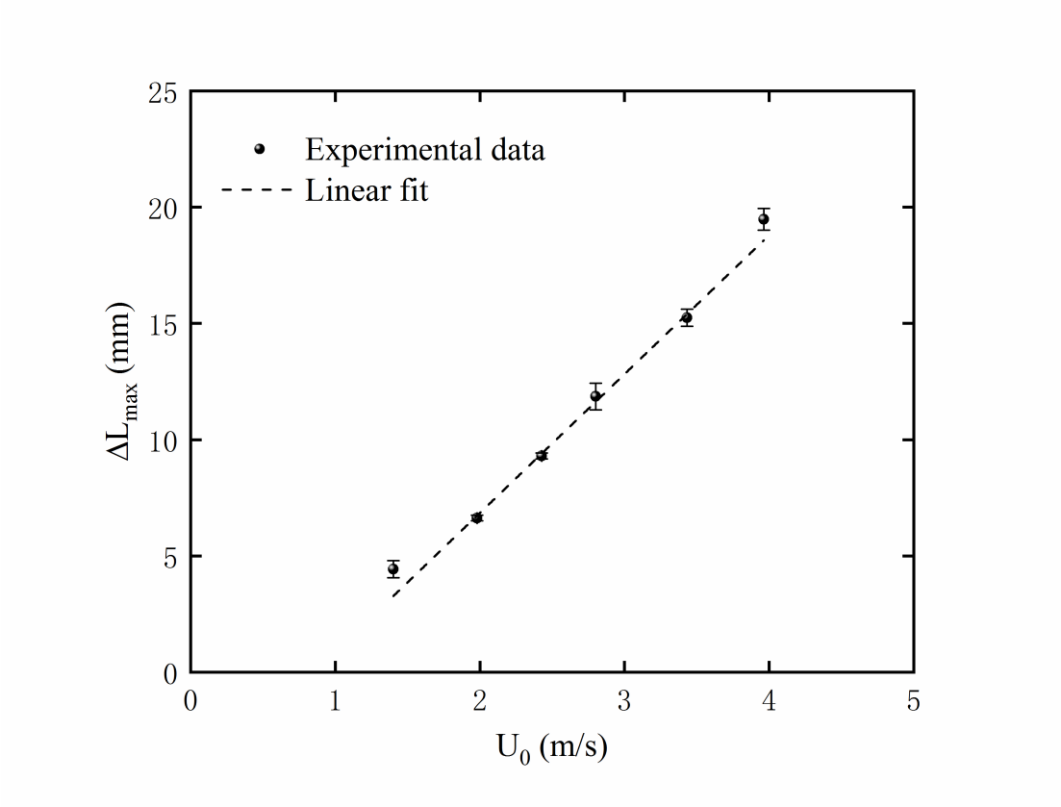


Fig. 11 Maximum compression ΔL_{max} as a function of the initial velocity U_0 for NCP during the initial stage of impact.

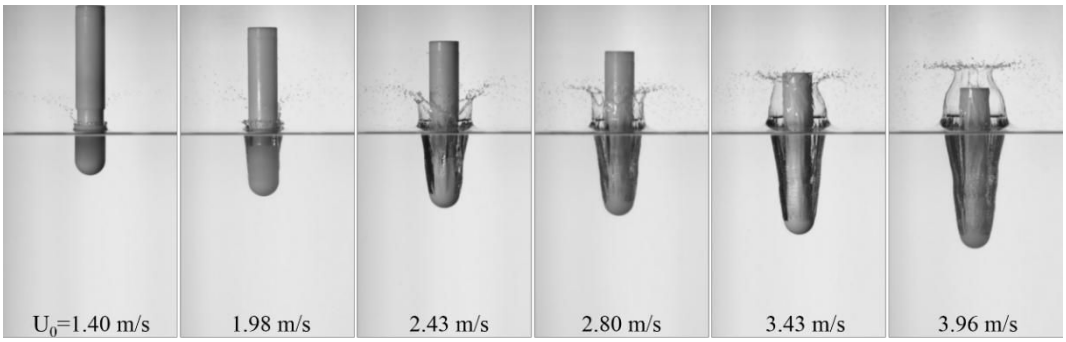


Fig. 12 Instantaneous water entry events of NCP with different initial velocities at the time of 32.5 ms

3.5. Force acting on the main body of NCP

To further understand the reason for the reduction of the maximum impact acceleration of NCP during the early stage of impact, a force analysis of the main body is presented in the following. As mentioned in Section 3.3, the pinch-off time of the cavity on the side of NCP was ~62 ms, which is

almost not affected by the compression of the nose and beyond the time range discussed. Even in low speed impact events, where no pinch-off occurs in the side of main body, no contact happened between the main body and the water before the nose reached maximum compression. Therefore, the forces acting on the main body can be shown in Fig. 13. A vertical force balance on the main body may be expressed as

$$m_b a = F_s + F_d + F_f - m_b g \tag{1}$$

where m_b represents the mass of the main body of projectile, a represents the absolute acceleration of the main body, F_s represents the force of spring acting on the main body, F_d represents the air drag, and F_f represents the frictional force between nose and main body. Ignoring the air drag F_d and assuming a very small friction F_f between the nose and the main body (which was considered at the beginning of the design to reduce this friction between them), Equation (1) can be simplified to:

$$m_b(a+g) = F_s \tag{2}$$

The force F_s is not clear in the process of the nose compression because the nose is not stationary and moving relative to the main body. Fortunately, the maximum impact acceleration experienced by the main body and the maximum compression of the nose appear almost at the same time and the compression remained constant a short time after reaching the maximum compression in all conducted tests. Therefore, a consistent motion state of the nose and the main body occurred and the force of spring acting on the main body F_s was thus equivalent to the force required to deform the spring, i.e., $F_s = \Delta L_{\max} \cdot K$, where $\Delta L_{\max}$ represents the maximum deformation of spring at different velocities and K represents the spring stiffness. Non-dimensionalizing Equation (2), the maximum impact acceleration $a_{\max}$ can be predict by:

$$\frac{a_{\max}}{g} = \frac{K \cdot \Delta L_{\max}}{m_b g} \tag{3}$$

where $a_{\max}$ is the measured value of maximum acceleration, and the relationship between absolute value and measured value is the absolute acceleration is equal to the measured acceleration minus the gravitational acceleration g, thus, here have:

$$a_{\max} = a_{a\max} - g \tag{4}$$

where a_{amax} is the maximum absolute acceleration.

The maximum measured acceleration a_{max} was normalized by g and plotted as a function of ΔL_{max} in Fig. 14. The dotted line indicates the prediction Equation (3). The experimental results basically coincide with theoretical predictions.

At the initial stage of water entry, the larger fluid force acts on the projectile in a short time, producing a large impulse and then resulting in a peak acceleration. When the spring is introduced between the nose and the main body, although the nose will suffer a large impact force, the deformation of the spring absorbs part of the impulse, thus reducing the peak value of the impact acceleration and delaying the occurrence time of the maximum impact acceleration. The larger initial impact force is transferred to the finite spring deformation in the form of energy conversion. Thus, the using of the spring can effectively reduce the peak acceleration during the early stage of impact.

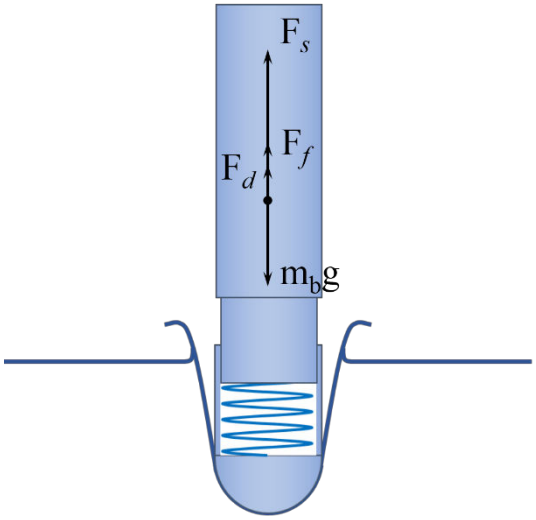


Fig. 13 Schematic diagram of force acting on the main body of the projectile during the initial stage of water entry.

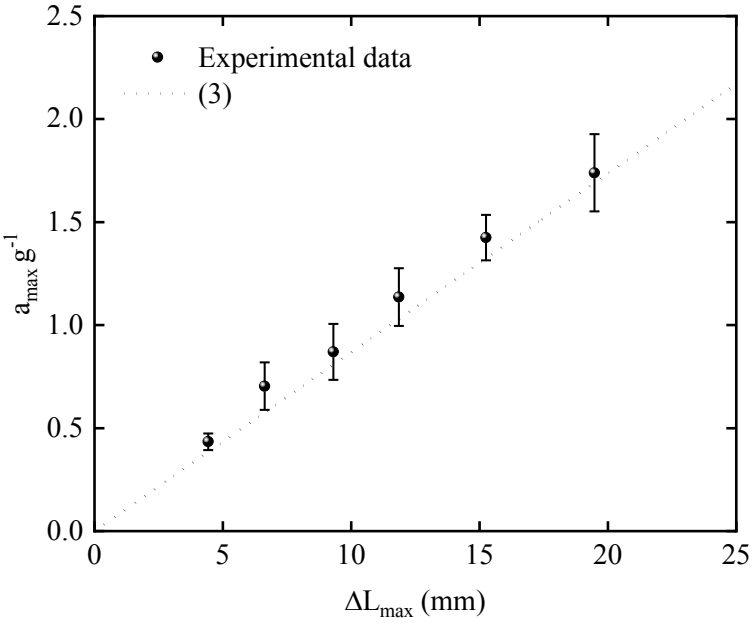


Fig. 14 Maximum impact acceleration a_{max} as a function of the maximum deformation ΔL_{max} for NCP during the initial stage of impact.

4. Conclusion

Water entry tests of two forms of slender projectiles were performed in this study. A peak impact acceleration for the nose fixed projectile (NFP) was found during the initial stage of water entry. The experimental results show that the maximum impact acceleration experienced by the NFP increased quadratically with the initial impact velocity during the early stage of impact. When a spring is introduced between the nose and the main body (NCP), the maximum impact acceleration increases linearly with the initial impact velocity and is significantly reduced at a relatively high initial velocity. For NCP, the time until the maximum impact acceleration is reached is ~32 ms, independent of the initial impact velocity. The time required for the nose to achieve maximum compression is also independent of the initial impact velocity and consistent with the maximum impact acceleration. The maximum compression increases linearly with increasing initial velocity. In addition, the nose compression spring increases the initial velocity required for the occurrence of cavity pinch-off events on the side of the main body. However, it slightly affects the non-dimensional pinch-off times of the cavity on the side of main body and the tail of the projectile. Finally, a simple prediction formula is established to indicate the relationship between the maximum impact acceleration and the maximum

nose compression. Compared to the test results, the maximum impact acceleration of the main body is only related to the maximum compression of the nose under the same spring stiffness. Since the deformation of the spring absorbs part of the impulse, thus decreasing the peak value of the impact acceleration and delaying the occurrence time of the maximum impact acceleration. This explained why the maximum impact acceleration can be effectively suppressed during the initial stage for NCP. This study has significant practical value for the design of objects to reduce the impact force they are exposed to during water entry.

Acknowledgements

This study was supported by the National Key Research and Development Program of China (Grant No. 2018YFA0703302), the National Natural Science Foundation of China (Grant No. 51575227, 51875243, 51706084), the Science and Technology Development Program of Jilin Province (Grant No.20180101319JC).

References

Alaoui, A.E., Nême, A., Scolan, Y.M., 2015. Experimental investigation of hydrodynamic loads and pressure distribution during a pyramid water entry. J. Fluids Struct. 54, 925–935.

Aristoff, J.M., Bush, J.W.M., 2009. Water entry of small hydrophobic spheres. J. Fluid Mech. 619, 45–78.

Aristoff, J.M., Truscott, T.T., Techet, A.H., Bush, J.W.M., 2010. The water entry of decelerating spheres. Phys. Fluids 22, 1–8.

Aristoff, J.M., Truscott, T.T., Techet, A.H., Bush, J.W.M., 2008. The water-entry cavity formed by low Bond number impacts. Phys. Fluids 20, 091111.

Bergmann, R., van der Meer, D., Gekle, S., van der Bos, A., Lohse, D., 2009. Controlled impact of a disk on a water surface: Cavity dynamics. J. Fluid Mech. 633, 381–409.

Bodily, K.G., Carlson, S.J., Truscott, T.T., 2014. The water entry of slender axisymmetric bodies. Phys. Fluids 26, 072108.

Chang, B., Croson, M., Straker, L., Gart, S., Dove, C., Gerwin, J., Jung, S., 2016. How seabirds plunge-dive without injuries. Proc. Natl. Acad. Sci. 113, 12006–12011.

Duclaux, V., Caillé, F., Duez, C., Ybert, C., Bocquet, L., Clanet, C., 2007. Dynamics of transient

cavities. J. Fluid Mech. 591, 1–19.

Duez, C., Ybert, C., Clanet, C., Bocquet, L., 2007. Making a splash with water repellency. Nat. Phys. 3, 180–183.

Dupeux, G., Goff, A. Le, Quéré, D., Clanet, C., 2010. The spinning ball spiral. New J. Phys. 12, 093004.

Glasheen, J.W., McMahon, T.A., 1996. Vertical water entry of disks at low Froude numbers. Phys. Fluids 8, 2078–2083.

Grady, R.J., 1979. Hydroballistics Design Handbook, Naval Sea Systems command Hydromechanics Committee.

Grumstrup, T., Keller, J.B., Belmonte, A., 2007. Cavity ripples observed during the impact of solid objects into liquids. Phys. Rev. Lett. 99, 1–4.

Hirano, Y., Miura, K., 1970. Water impact accelerations of axially symmetric bodies. J. Spacecr. Rockets 7, 762–764.

Korobkin, A.A., Pukhnachov, V. V., 1988. Initial stage of water impact. Annu. Rev. Fluid Mech. 20, 159–185.

Korobkin, A.A., Scolan, Y.M., 2006. Three-dimensional theory of water impact. Part 2. Linearized Wagner problem. J. Fluid Mech. 549, 343–373.

Lee, M., Longoria, R.G., Wilson, D.E., 1997. Cavity dynamics in high-speed water entry. Phys. Fluids 9, 540–550.

May, A., 1975. Water Entry and the Cavity-Running Behavior of Missiles. Weapons Cent., White Oak Lab, MD. Tech. Rep. 20910, Nav. Surf.

Moghisi, M., Squire, P.T., 1981. An experimental investigation of the initial force of impact on a sphere striking a liquid surface. J. Fluid Mech. 108, 133–146.

Rosellini, L., Hersen, F., Clanet, C., Bocquet, L., 2005. Skipping stones. J. Fluid Mech. 543, 137–146.

Shiffman, M., Spencer, D.C., 1951. The force of impact on a cone striking a water surface (vertical entry). Commun. Pure Appl. Math. 4, 379–417.

Shiffman, M., Spencer, D.C., 1945. The force of impact on a sphere striking a water surface (second approximation). AMP Rep. 42.2R, AMG-NYU No. 133.

Speirs, N.B., Belden, J., Pan, Z., Holekamp, S., Badlissi, G., Jones, M., Truscott, T.T., 2019. The water entry of a sphere in a jet. J. Fluid Mech. 863, 956–968.

Thoroddsen, S.T., Etoh, T.G., Takehara, K., Takano, Y., 2004. Impact jetting by a solid sphere. J. Fluid Mech. 499, 139–148.

Truscott, T.T., Techet, A.H., 2009a. Water entry of spinning spheres. J. Fluid Mech. 625, 135–165.

Truscott, T.T., Techet, A.H., 2009b. A spin on cavity formation during water entry of hydrophobic and hydrophilic spheres. Phys. Fluids 21, 1–4.

Tveitnes, T., Fairlie-Clarke, A.C., Varyani, K., 2008. An experimental investigation into the constant velocity water entry of wedge-shaped sections. Ocean Eng. 35, 1463–1478.

Von Karman, T., 1929. The impact of seaplane floats during landing. Tech. Rep. 321. Natl. Advis. Comm. Aeronaut., Washington, DC.

Wagner, H., 1932. Phenomena associated with impacts and sliding on liquid surfaces. J. Appl. Math. Mech. 12, 193–215.

Wang, T.M., Yang, X.B., Liang, J.H., Yao, G.C., Zhao, W.D., 2013. CFD based investigation on the impact acceleration when a gannet impacts with water during plunge diving. Bioinspiration and Biomimetics 8, 036006.

Worthington, A.M., Cole, R.S., 1897. Impact with a Liquid Surface, Studied by the Aid of Instantaneous Photography. Philos. Trans. R. Soc. A Math. Phys. Eng. Sci. 189, 137–148.

Yu, Y.T., 1945. Virtual masses of rectangular plates and parallelepipeds in water. J. Appl. Phys. 16, 724–730.

* Corresponding author:

Chengchun Zhang[a,b,*], E-mail: jluzcc@jlu.edu.cn



https://dspace.org/

Water entry of slender segmented projectile connected by spring

Wu, Zhengyang; Zhang, Chengchun; Wang, Jing; Shen, Chun; Yang, Liang ...

2020-09-16
Elsevier
https://doi.org/10.1016/j.oceaneng.2020.108016
Wu Z, Zhang C, Wang J, et al., (2020) Water entry of slender segmented projectile connected by spring. Ocean Engineering, Volume 217, December 2020, Article number 108016

Downloaded from a DSpace repository. https://dspace.org/